EDGE ARTICLE

Check for updates

One-pot cascade construction of nonsubstituted quinoline-bridged covalent organic frameworks†

Huaji Pang,[ab] Dekang Huang, [ID][a] Yanqiu Zhu,[ab] Xiaodong Zhao[ab] and Yonggang Xiang [ID] *[ab]

Irreversible locking of imine linkages into stable linkages represents a promising strategy to improve the robustness and functionality of covalent organic frameworks (COFs). We report, for the first time, a multi-component one-pot reaction (OPR) for imine annulation to construct highly stable nonsubstituted quinoline-bridged COFs (NQ-COFs), and that equilibrium regulation of reversible/irreversible cascade reactions by addition of $MgSO_4$ desiccant is crucial to achieve high conversion efficiency and crystallinity. The higher long-range order and surface area of NQ-COFs synthesized by this OPR than those of the reported two-step post-synthetic modification (PSM) facilitate charge carrier transfer and photogeneration ability of superoxide radicals ($O_2^{\cdot-}$), which makes these NQ-COFs more efficient photocatalysts for $O_2^{\cdot-}$ mediated synthesis of 2-benzimidazole derivatives. The general applicability of this synthetic strategy is demonstrated by fabricating 12 other crystalline NQ-COFs with a diversity of topologies and functional groups.

Introduction

Covalent organic frameworks (COFs) are a unique class of polymer materials that are fabricated by atomically connecting building blocks with one another through covalent bonds.[1–3] With a periodic structure, high accessible surface area, well-defined porosity, and designable construction, COFs are burgeoning as a new research frontier in energy storage,[4,5] separation,[6,7] sensing,[8–10] and catalysis.[11–15] It is well recognized that the reversibility of the covalent linkages serves as the major driving force for the formation of long-range ordered COFs. This dynamic nature of the bonds, however, has a negative impact on the chemical stability of COFs, thus giving rise to an unavoidable trade-off between crystallinity and robustness.[16] To address this intractable issue, the past few years have witnessed growing interest in the exploitation of efficient methodologies to improve the stability of COFs.[17–23]

One of the methodologies to construct ultrastable COFs is to chemically convert reversible covalent linkages into irreversible robust ones by post synthetic modification (PSM).[24,25] For instance, C=N bonds in imine-linked COFs could be transformed to more robust amide linkages under an oxidizing condition with high conversion efficiency and crystallinity.[26–29] Similarly, locking of the imine linkage by other organic

reactions could afford stable benzothiazole,[30,31] quinoline,[32–35] and benzoxazole linkages,[36] and C–N bonds.[37,38] Following these pioneering works, we recently reported a novel oxidant-free PSM method to construct ultrastable nonsubstituted quinoline-linked COFs (labelled as NQ-COFs) *via* rhodium-catalyzed [4 + 2] annulation.[34] However, these PSM strategies, including ours, still suffer from some drawbacks, such as collapse of the framework and decreased crystallinity during the solid-state transformation, which might hamper the separation and transfer of photoinduced electron–hole pairs when these PSM derived COFs are applied in photocatalytic processes. Therefore, although the NQ-COFs synthesized in our work have demonstrated their first application in photoredox organic transformation, there is still much room to boost their photocatalytic activities. One-pot reaction (OPR) is considered a possible solution to the above dilemma, because such a methodology allows the building of ordered oligomeric structures from the very beginning of the reaction and thus is expected to produce more highly crystalline frameworks.[39–45] However, examples of producing ultrastable COFs through OPR are rare, because balancing the cascade reaction conditions between reversible imine formation and subsequent irreversible locking is extremely challenging.

In this contribution, we successfully realized the one-pot synthesis of NQ-COFs after extensive screening of reaction conditions. It was found that the addition of $MgSO_4$ was crucial to complete imine locking and form high crystallinity NQ-COFs. Detailed characterization indicated that a more ordered framework and higher surface area were obtained for the NQ-COFs synthesized by OPR than the ones synthesized by PSM,

[a]Department of Chemistry, College of Science, Huazhong Agricultural University, Wuhan, Hubei, 430070, China. E-mail: ygxiang@mail.hzau.edu.cn

[b]College of Resources and Environment, Huazhong Agricultural University, 430070, Wuhan, P. R. China
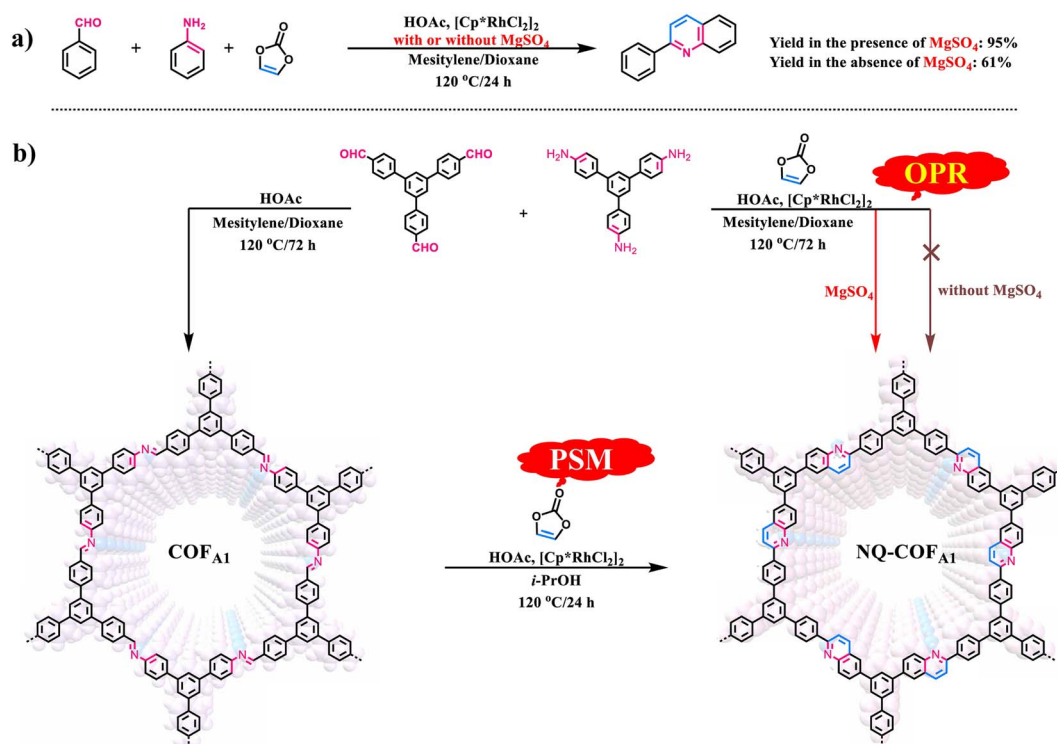
and these properties were beneficial to the exposure of active sites and charge carrier transfer. As a result, the NQ-COF obtained by OPR displayed superior photocatalytic performance for driving the $O_2^{\bullet-}$ mediated synthesis of 2-benzimidazole derivatives. By means of this newly developed strategy, 12 other NQ-COFs were also obtained, substantiating its general applicability.

Results and discussion

Given that OPR has obvious advantages over PSM for preparation of COFs, particularly those containing structural diversity and complexity, we made a rapid attempt to synthesize **NQ-COF$_{A1}$** via OPR under the reported PSM reaction conditions. However, it failed with only amorphous polymer obtained (Scheme 1b). Such reaction conditions were also not suitable for the smooth operation of the model reaction, as only a 61% yield of 2-phenylquinoline was achieved (Scheme 1a). To drive the multicomponent reaction, extensive screening of reaction conditions was conducted (supplementary Table 1†). It was found that the presence of MgSO$_4$ was essential in constructing highly crystalline frameworks, and all experiments aiming to crystallize **NQ-COF$_{A1}$** were proven to be unsuccessful if MgSO$_4$ was absent. Next, the amount of MgSO$_4$ was screened, whereby MgSO$_4$ (1.0, 2.0, 4.0, 6.0 and 10.0 equiv. per imine) was added in the process of synthesizing **NQ-COF$_{A1}$-OPR**. It turned out that a low conversion efficiency was observed with a great amount of unreacted imine and aldehyde in the presence of 1.0 and 2.0 equivalents of MgSO$_4$ according to Fourier transform infrared

(FT-IR) measurements, and a high conversion efficiency was achieved when 4.0, 6.0 and 10.0 equivalents of MgSO$_4$ were added (supplementary Fig. 2a†). However, it was found that addition of 4.0 equivalents of MgSO$_4$ resulted in the strongest powder X-ray diffraction (PXRD) intensity (supplementary Fig. 2b†). Inspired by this result, another typical desiccant, CaCl$_2$ (4.0 equiv. per imine), was also used instead of MgSO$_4$, however a low conversion efficiency and complete loss of crystallinity were observed via FT-IR and PXRD measurements (supplementary Fig. 3†). The optimal reaction conditions to obtain **NQ-COF$_{A1}$** were determined to be as follows: vinylene carbonate (3.0 equiv. per imine), [Cp*RhCl$_2$]$_2$ (1.5 mol% per imine), MgSO$_4$ (4.0 equiv. per imine), HOAc (50 μL), reaction temperature of 120 °C, reaction time of 3 days, and a mixed solvent system of mesitylene/dioxane (1 : 2, v/v). Under these reaction conditions, the yield of model compound 2-phenylquinoline was also greatly increased to 95%, further verifying the significant role of MgSO$_4$. It is known that the mechanism for the construction of nonsubstituted quinoline linkages starts with the formation of imine by condensation of aldehyde and amine, followed by Rh-catalyzed [4 + 2] annulation between the in situ generated imine and vinylene carbonate. To form an ordered structure, the reversible Schiff-base reaction must be fast enough to promote error correction before locking by the subsequent irreversible annulation reaction. The drying agent MgSO$_4$ was regarded as crucial in the first step of reversible Schiff-base reaction, as the in situ generated water could be removed to accelerate the formation rate of imine intermediates. The water content with or without addition of MgSO$_4$ in

Scheme 1 (a) Synthesis of model compound 2-phenlyquinoline via multicomponent reactions with or without addition of MgSO$_4$. (b) Construction of **NQ-COF$_{A1}$** via OPR and PSM methods.

the reaction solution was determined by Karl Fisher titration, and the results indicated that the content of water in the solution for preparing COF_{A1} was 4.0 times that for preparing NQ-COF_{A1}-OPR (supplementary Tables 4–6†). Therefore, the role of $MgSO_4$ is speculated to adjust the balance between reversible Schiff-base reaction and irreversible annulation reaction. It is noted that, for simplicity in illustration, the NQ-COF_{A1} samples prepared by OPR and PSM are labelled as NQ-COF_{A1}-OPR and NQ-COF_{A1}-PSM in this work, respectively.

The long-range ordered structure of NQ-COF_{A1}-OPR was verified using PXRD measurement. As shown in Fig. 1a, the PXRD pattern of NQ-COF_{A1}-OPR shows six prominent diffraction peaks at 4.0°, 7.0°, 8.0°, 10.6°, 14.5°, and 25.6°, which are assigned to the (100), (110), (020), (210), (400), and (001) facets, respectively. Using the optimized monolayer structure, the simulated eclipsed (AA) stacking in the space group $P1$ was found to fit very well with the experimental PXRD pattern, and Pawley refinement of the crystal model afforded the unit cell of $\alpha = \beta = 90°$, $\gamma = 120°$, $a = 25.47$ Å, $b = 26.22$ Å, $c = 3.59$ Å with satisfactory R-factors ($R_p = 1.1\%$, $R_{wp} = 1.49\%$). In comparison, NQ-COF_{A1}-PSM shows a similar PXRD pattern to NQ-COF_{A1}-OPR but an obviously lower intensity of the peaks. Meanwhile, the (100) peak of NQ-COF_{A1}-OPR has a narrower full-width at half-maximum (FWHM) value of 0.47° than that of NQ-COF_{A1}-PSM (0.49°), also suggesting a higher crystallinity of NQ-COF_{A1}-OPR. It can be seen that an amorphous polymer was obtained with no obvious PXRD peaks in the absence of $MgSO_4$. The more ordered crystal structure of NQ-COF_{A1}-OPR over NQ-COF_{A1}-PSM was also revealed by N_2 adsorption–desorption measurements

at 77 K (Fig. 1b). The adsorption profiles of all three COFs display reversible type IV isotherms, which are typical of mesoporous materials, and the narrow pore size distributions of COF_{A1}, NQ-COF_{A1}-OPR, and NQ-COF_{A1}-PSM were determined by the non-local density flooding theory (NLDFT) fitted curves to be centered at 2.8, 2.6, and 2.6 nm, respectively, in good agreement with their simulated structures (supplementary Fig. 4†). Significantly, the Brunauer–Emmett–Teller (BET) specific surface areas of COF_{A1}, NQ-COF_{A1}-OPR, and NQ-COF_{A1}-PSM were determined to be 1377, 1211, and 964 m^2 g^{-1}, respectively, which are 68%, 68%, and 54% of the theoretical values of COF_{A1} (2028 m^2 g^{-1}) and NQ-COF_{A1} (1779 m^2 g^{-1}). This result clearly indicates that the PSM strategy decreases the surface area of COF_{A1} as a result of some unavoidable factors. The OPR strategy can endow NQ-COF_{A1} with a higher surface area because NQ-COF_{A1}-OPR has higher crystallinity and less amorphous monomer in the framework pores.

Considering that PSM and OPR afforded NQ-COF_{A1} with a similar conversion efficiency, the more ordered periodic structure of NQ-COF_{A1}-OPR may arise from the different mechanism of crystallization. The morphologies were then studied using field emission scanning electron microscopy (SEM). As shown in Fig. 1e, COF_{A1} was obtained in the form of layer-like blocks with a smooth surface, and the imine locking by the heterogeneous PSM has no significant impact on the morphology. In sharp contrast, NQ-COF_{A1}-OPR is composed of irregular coral-like lamellae decorated on the outer ring of nanosheets with a relatively rough surface, which may contribute to more exposure of surface area. Based on the above
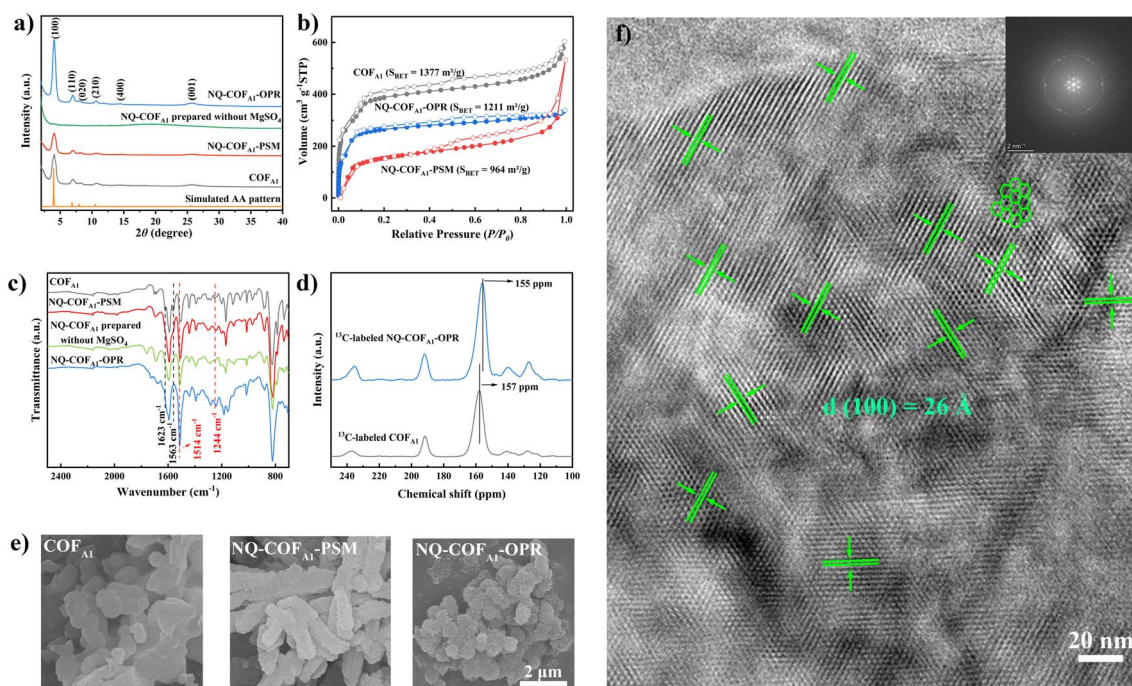

Fig. 1 (a) Experimental PXRD patterns of COF_{A1}, NQ-COF_{A1}-OPR, and NQ-COF_{A1}-PSM. The simulated PXRD pattern was generated using NQ-COF_{A1}-OPR. (b) N_2 sorption isotherm curves of COF_{A1}, NQ-COF_{A1}-OPR, and NQ-COF_{A1}-PSM. (c) FT-IR spectra of COF_{A1}, NQ-COF_{A1}-OPR, and NQ-COF_{A1}-PSM. (d) Solid-state isotopically enriched ^{13}C CP/MAS NMR spectra. (e) SEM images of COF_{A1}, NQ-COF_{A1}-OPR, and NQ-COF_{A1}-PSM. (f) HRTEM image of NQ-COF_{A1}-OPR. Inset: fast Fourier transform (FFT) pattern.

result, we assumed that the more rigid skeleton of the quinoline-based oligomers than imine-based counterparts formed from the very beginning may enhance the interlayer π–π stacking, which can act as an impetus to drive the formation of a more ordered periodic structure with high crystallinity. This was further clearly visualized by high-resolution transmission electron microscopy (HRTEM) (Fig. 1f), and a well-ordered arrangement of continuous honeycomb-like pore channels was observed to extend through the whole crystal domain. The hexagonal shape with a pore size of 26 Å is in good consistence with the simulated AA-stacking mode of **NQ-COF$_{A1}$-OPR**. Meanwhile, the ordered layered π–π stacking structure along the (001) direction can also be observed with an interlayer distance of 3.59 Å (supplementary Fig. 5†).

As it was previously reported that Rh-catalyzed annulation of imine by the PSM strategy could achieve quantitative conversion, we first compared the FT-IR spectra of **NQ-COF$_{A1}$-OPR** and **NQ-COF$_{A1}$-PSM**. The complete disappearance of the characteristic imine stretching vibration at 1623 cm^{-1} for **NQ-COF$_{A1}$-PSM** verifies the high conversion efficiency (Fig. 1c). Satisfactorily, **NQ-COF$_{A1}$-OPR** shows an almost identical spectrum to that of **NQ-COF$_{A1}$-PSM**. On the other hand, there is still an obvious residue of C=N bonds in **NQ-COF$_{A1}$** without MgSO$_4$ addition, confirming that OPR can only smoothly operate in the presence of MgSO$_4$. Subsequently, isotopically enriched ^{13}C-labeled aldehyde was synthesized. After the structure was verified using FT-IR spectra (supplementary Fig. 6†), the ^{13}C-labeled **COF$_{A1}$** and **NQ-COF$_{A1}$-OPR** were afforded under the same conditions for collecting the solid-state ^{13}C cross-polarization magic angle rotation (CP-MAS) NMR spectra. As shown in Fig. 1d, the imine carbon peak in ^{13}C-labeled **NQ-COF$_{A1}$-OPR** at 157 ppm disappears completely while a new peak appears at 155 ppm for the quinoline carbon of ^{13}C-labeled **NQ-COF$_{A1}$-OPR**. The formation of the quinoline-linked COF was further supported by high-resolution X-ray photoelectron spectroscopy (XPS) analysis as the binding energy of N 1s in C=N fragments shifts up from ~398.9 eV to ~399.2 eV (supplementary Fig. 7†). The above measurements revealed that both the formation of reversible imine and subsequent Rh-catalyzed annulation in the multi-component OPR collaborated very well in the presence of MgSO$_4$.

The chemical stability of the NQ-COFs was evaluated by subjecting **COF$_{A1}$** and **NQ-COF$_{A1}$-OPR** to several harsh chemical conditions for 24 hours, including a strong acid (12 M HCl at 60 °C, 98% trifluoroacetic acid at 60 °C), strong base (14 M NaOH in H$_2$O/MeOH at 60 °C), and strong reducing agent (NaBH$_4$ in MeOH at 60 °C). It was found that the crystallinity of **NQ-COF$_{A1}$-OPR** was retained well according to PXRD measurements whereas **COF$_{A1}$** became amorphous, proving the robust nature of the frameworks of **NQ-COF$_{A1}$-OPR**. Both COFs were also treated with *n*-hexylamine solution at 120 °C for 24 hours (supplementary Fig. 8†). Aminolysis of the imine bridges in **COF$_{A1}$** converted the suspension into a transparent state; however, the quinoline linkages were not affected. In addition, the thermal stability of the COFs was studied using thermogravimetric analysis (TGA), and the thermal decomposition

temperature of **NQ-COF$_{A1}$-OPR** was found to be higher than that of **NQ-COF$_{A1}$-PSM** (supplementary Fig. 9†).

To demonstrate the generality of OPR for COF synthesis, a range of building blocks with different skeletons and geometries was utilized to construct NQ-COFs following the topology design principle (Fig. 2). After extensive optimization of polycondensation conditions, the combination of [3 + 2] and [3 + 3] can afford six hexagonal NQ-COFs (**NQ-COF$_{B1}$**, **NQ-COF$_{B2}$**, **NQ-COF$_{C1}$**, **NQ-COF$_{C2}$**, **NQ-COF$_{F1}$**, and **NQ-COF$_{F2}$**) with mesoporous or microporous structures in yields of 89–95%. All of them display high crystallinity according to PXRD measurements, and the diffraction patterns were found to be in good agreement with the eclipsed AA-stacking model. On the other hand, **NQ-COF$_{D4}$**, **NQ-COF$_{D5}$**, and **NQ-COF$_{F3}$** with rhombic pores were also constructed with high crystallinity and yields using the [4 + 2] combination. Moreover, we successfully synthesized three functional NQ-COFs (**NQ-COF$_{E4}$**, **NQ-COF$_{E5}$**, and **NQ-COF$_{G1}$**) starting from substituted aromatic building blocks, which might provide more opportunities for NQ-COFs to be applied in wide areas in the future. 12 of the corresponding imine-linked COFs were also synthesized to confirm the high locking efficiency using FT-IR spectra and XPS analysis (supplementary Fig. 10 and 11†). Meanwhile, all the NQ-COFs displayed smaller BET specific surface areas and narrower pore size distributions than the corresponding imine-linked COFs, and this trend is also consistent with the comparison between **COF$_{A1}$** and **NQ-COF$_{A1}$-OPR** (supplementary Fig. 12 and 13†). The robust skeletons of these NQ-COFs were confirmed using PXRD and FT-IR measurements before and after aminolysis tests (supplementary Fig. 14 and 15†). SEM observation revealed that the NQ-COFs displayed different morphologies from the corresponding imine-linked COFs, which might arise from the different crystallization process (supplementary Fig. 16†). Furthermore, all these 12 NQ-COFs were also characterized using HRTEM, and their high crystallinities were also demonstrated (supplementary Fig. 17†).

As we previously reported that enhanced π-electron delocalization of NQ-COFs favors visible-light absorption and carrier transfer in comparison to imine-linked COFs, it is particularly important to further clarify the effects of crystallinity and surface area differences of **NQ-COF$_{A1}$** synthesized by the PSM and OPR strategies on the photophysical properties. Ultraviolet-visible diffuse reflectance spectroscopy (UV-vis DRS) measurements revealed that quinoline formation contributes to the redshifted absorption, but **NQ-COF$_{A1}$-OPR** displays a longer absorption onset than **NQ-COF$_{A1}$-PSM**. The optical energy bandgap (E_g) of **COF$_{A1}$**, **NQ-COF$_{A1}$-PSM**, and **NQ-COF$_{A1}$-OPR** was calculated from the Tauc plots to be 2.64, 2.36, and 2.15 eV, respectively (Fig. 3a). The superior light absorption of **NQ-COF$_{A1}$-OPR** may arise from more efficient in-plane π-conjugation.[46] Due to the positive nature of the slopes of the plots obtained at different frequencies by Mott–Schottky (MS) measurements, the flat-band potential (E_{fb}) of the n-type **COF$_{A1}$**, **NQ-COF$_{A1}$-PSM**, and **NQ-COF$_{A1}$-OPR** was determined from the *x*-axis intercepts of the MS plots to be −1.03, −1.01, and −0.99 V (*vs.* Ag/AgCl), respectively (Fig. 3b, supplementary Fig. 18†). Considering that the CB potential of n-type semiconductors is
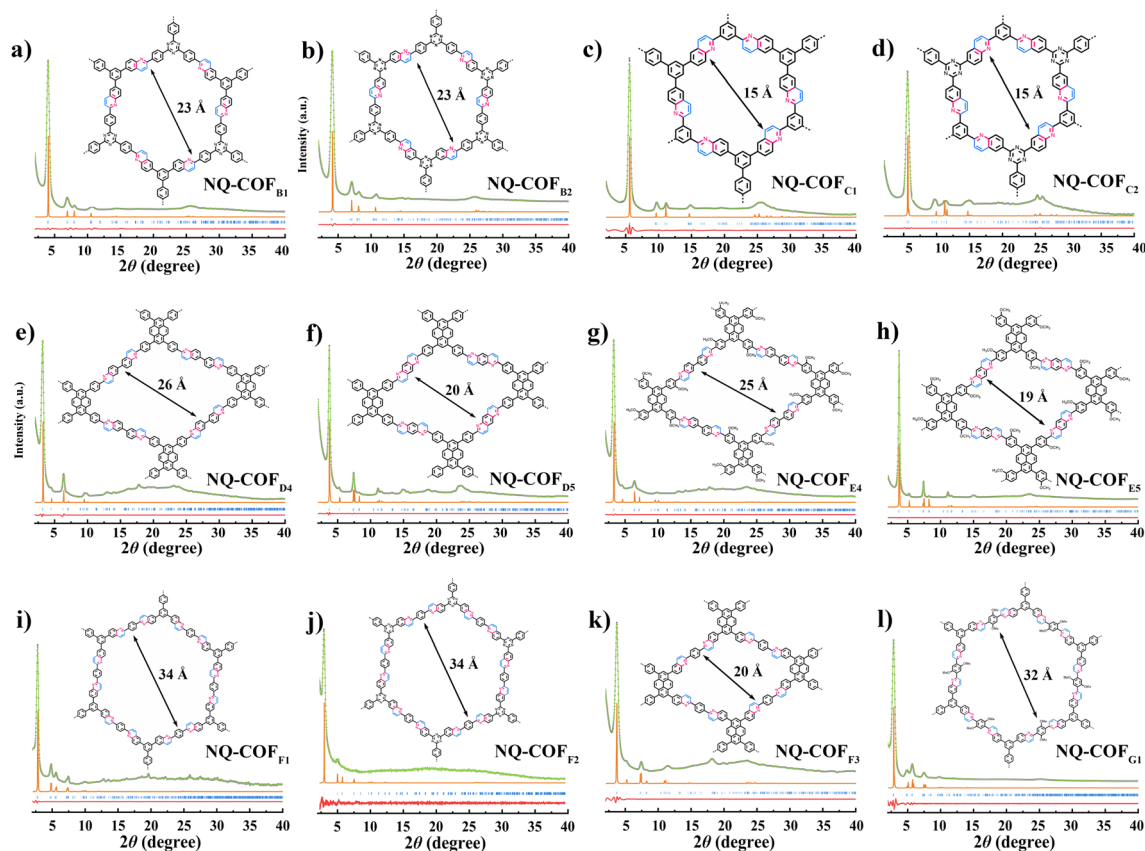
Fig. 2 XRD patterns of 12 different NQ-COFs (a–l). Green dot: experimental data, green line: Pawley refined profiles, orange line: simulated patterns of eclipsed (AA) stacking, blue bar: Bragg positions, and claret line: refinement differences.

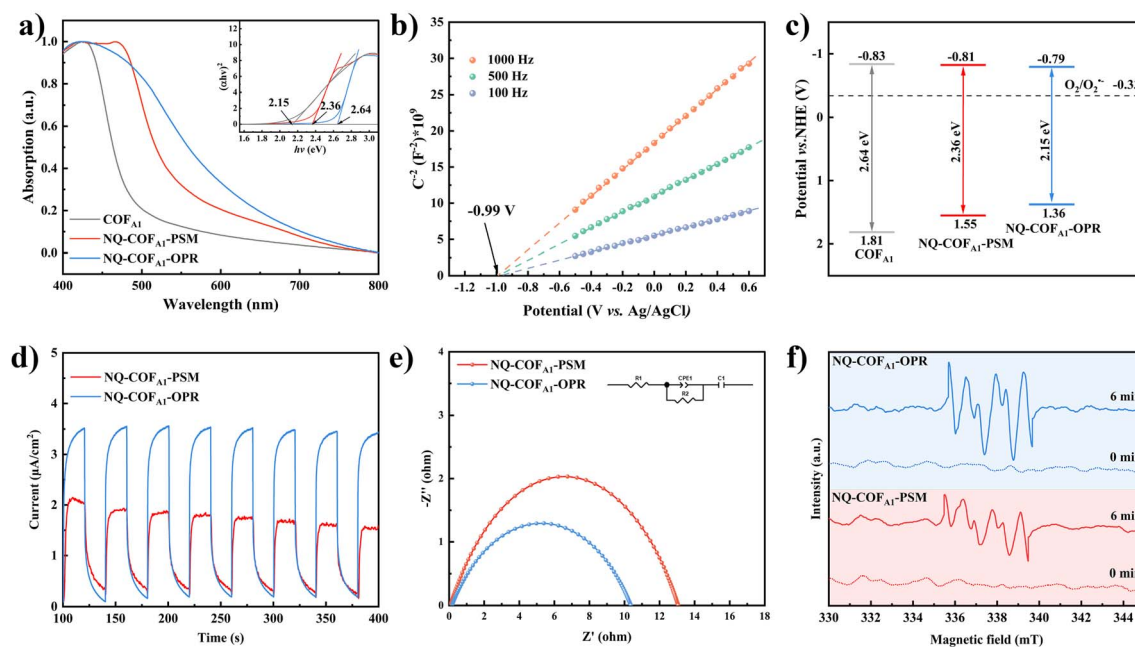**Fig. 3** (a) UV-vis DRS. The inset shows the corresponding Tauc plots. (b) Mott–Schottky plots of **NQ-COF$_{A1}$-OPR**. (c) Energy band structure diagram. (d) Transient photocurrents. (e) EIS spectra. (f) EPR spectra of the DMPO-O$_2$$^{\bullet-}$ adduct in the dark and under visible light irradiation.

almost equal to the flat-band potential, the conduction band (CB) potentials of **COF$_{A1}$**, **NQ-COF$_{A1}$-PSM**, and **NQ-COF$_{A1}$-OPR** are equal to -0.83, -0.81, and -0.79 V (*vs.* NHE), respectively. Combining the E_g and CB values, the valence band (VB) positions of **COF$_{A1}$**, **NQ-COF$_{A1}$-PSM**, and **NQ-COF$_{A1}$-OPR** were calculated to be 1.81, 1.55, and 1.36 V (*vs.* NHE), respectively. Accordingly, all these three COFs have the ability of photogeneration of superoxide radicals ($O_2^{\bullet-}$) from O_2 (Fig. 3c).

Furthermore, several other techniques were utilized to verify the superior photogenerated carrier transfer efficiency. In the transient photocurrent response measurements, **NQ-COF$_{A1}$-OPR** also has the stronger photocurrent intensity (Fig. 3d). On the other hand, a smaller arc radius was obtained for **NQ-COF$_{A1}$-OPR** than **NQ-COF$_{A1}$-PSM** by electrochemical impedance spectroscopy (EIS) measurements (Fig. 3e). Based on these initial results, we attempted to evaluate the reduction ability of O_2 to $O_2^{\bullet-}$ driven by photogenerated electrons using paramagnetic spectra (EPR), and it turned out that the characteristic peaks of $O_2^{\bullet-}$ could be observed when both suspended samples in CH_3CN in the presence of 5,5-dimethyl-1-pyrroline *N*-oxide (DMPO) were irradiated for 6 min by a 300 W Xe lamp. **NQ-COF$_{A1}$-OPR** has the stronger ability for $O_2^{\bullet-}$ generation, which should be conducive to its higher efficiency in $O_2^{\bullet-}$-mediated photocatalytic organic reactions (Fig. 3f).

Inspired by the superior potential of **NQ-COF$_{A1}$-OPR** to reduce O_2 to the reactive oxygen species (ROS) $O_2^{\bullet-}$, we attempted to apply **NQ-COFs** as photocatalysts in the $O_2^{\bullet-}$-mediated coupling of aryl diamine and aryl aldehyde for generation of the versatile building block benzimidazole.[47] Phenylenediamine (**1a**) and benzaldehyde (**2a**) were selected as the model reactants for the initial reaction condition optimization (Fig. 4a). The desired product 2-phenyl-1*H*-benzo[*d*]imidazole (**3a**) could be obtained in 97% yield in the mixed solvent system EtOH/H$_2$O with **NQ-COF$_{A1}$-OPR** as the photocatalyst and an 18 W blue LED (460–465 nm) lamp as the light source under an O_2 atmosphere. When the reaction time was prolonged to 36 h, the yield remained the same, and no product was detected in the absence of oxygen or light, proving the pivotal role of photogenerated ROS. In sharp contrast, 50% and 69% yields of the target product were afforded when **COF$_{A1}$** and **NQ-COF$_{A1}$-PSM** were used as the photocatalysts under the same reaction conditions. Firstly, this revealed that the quinoline linkage helps to address the limited in-plane π-electron delocalization. More importantly, the more ordered framework of **NQ-COF$_{A1}$-OPR** is indeed more beneficial to the transfer of photogenerated electrons and thus the generation of ROS is accelerated in comparison to **NQ-COF$_{A1}$-PSM**, which correlates with the EPR results. With the optimized reaction conditions in hand, a variety of substituted phenylenediamines were tested to explore the coupling scope (Fig. 4b), and it was found that phenylenediamines 3,4-substituted with electron-deficient (3,4-F$_2$, 3,4-Cl$_2$ and 3-F) or electron-deficient (3-Me) groups were tolerated in the reaction, and the desired products **3b–3e** could be obtained in good yields. Furthermore, the coupling reaction
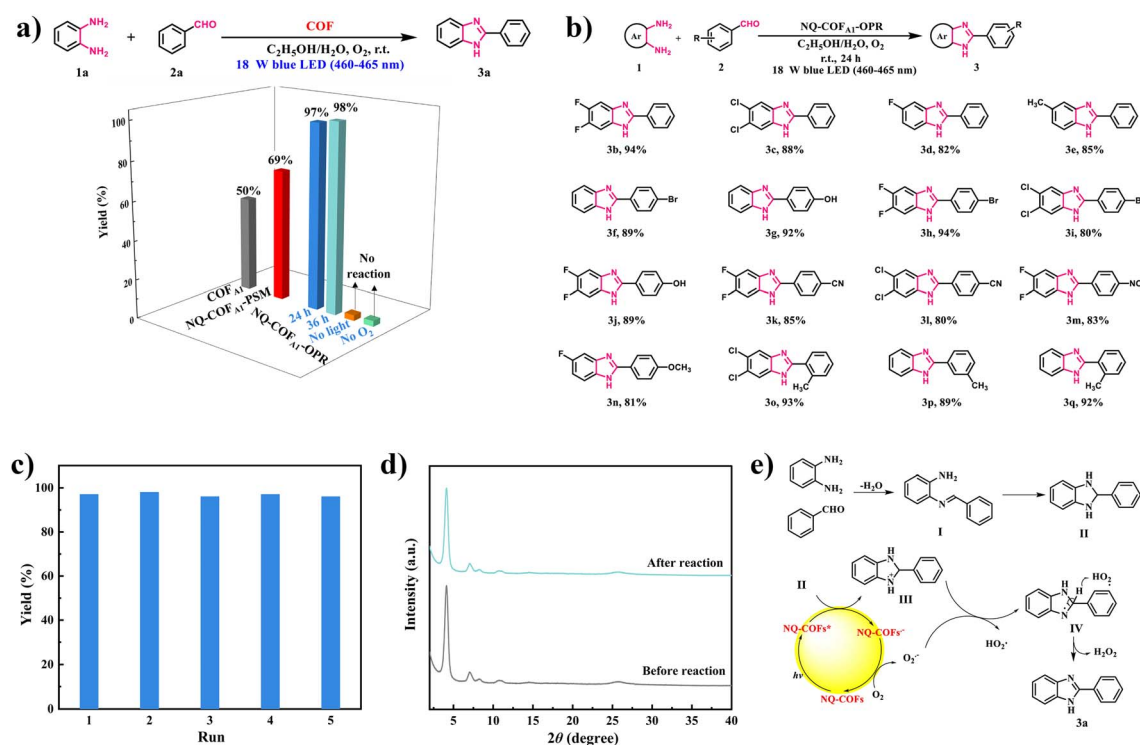

Fig. 4 (a) Screening and comparison of reaction conditions for the synthesis of the model compound 2-phenyl-1*H*-benzo[*d*]imidazole. Standard conditions: **1a** (0.5 mmol), **2a** (0.5 mmol), COF (5 mg), EtOH/H$_2$O (1 mL/1 mL), 18 W blue LED (460−465 nm), and 24 h. (b) Substrate scope for the synthesis of 2-benzimidazole using **NQ-COF$_{A1}$-OPR** as the photocatalyst under standard reaction conditions. (c) Long-term stability obtained by recycling experiments. (d) PXRD comparison before and after five runs of the photocatalytic reaction. (e) Proposed mechanism for the photocatalytic reaction.

also ended in a good conversion efficiency when benzaldehyde was substituted at the *ortho-*, *meta* or *para*-position (*p*-Br, *p*-OH, *p*-CN, *p*-NO$_2$, *p*-OCH$_3$, *o*-Me, and *m*-Me) (**3f–3q**) under the standard conditions.

Another advantage of heterogeneous photocatalytic reaction is the facile recycling of the photocatalyst for repeated runs without activity decay. Taking the model reaction for the generation of **3a** as an example, **NQ-COF$_{A1}$-OPR** could be easily separated by filtration after the reaction ended every time. After being washed and dried, the recycled **NQ-COF$_{A1}$-OPR** was directly used for the next run, and it turned out that a 96% yield of **3a** was still obtained after the fifth recycling reaction, proving its high photochemical stability (Fig. 4c). Meanwhile, the high stability of **NQ-COF$_{A1}$-OPR** was further supported by PXRD and FT-IR data, which confirmed that the chemical structure and robust framework could be retained after the reaction (Fig. 4d and supplementary Fig. 19†).

To gain deep insight into the mechanism of the coupling reaction, experiments featuring ROS trapping were designed. When the singlet oxygen ($^1O_2$) scavenger β-carotene (3 mg) was added into the reaction, a 96% yield of **3a** in the model reaction was obtained without other conditions changed. On the other hand, no product was detected in the presence of the $O_2^{\bullet-}$ scavenger *p*-benzoquinone (3 mg), proving that $O_2^{\bullet-}$ was the dominant active species. Based on the above observations and a previous report, a plausible reaction mechanism was proposed, as shown in Fig. 4e. **NQ-COF$_{A1}$-OPR** is converted to the photoexcited **NQ-COFA1-OPR***, and the cyclized intermediate **II** of imine **I** acts as the electron donor to **NQ-COF$_{A1}$-OPR*** for the generation of **NQ-COF$_{A1}$-OPR•$^-$** and intermediate **III**. Next, O_2 is activated by **NQ-COF$_{A1}$-OPR•$^-$** to afford the active species $O_2^{\bullet-}$ along with the ground state **NQ-COF$_{A1}$-OPR**, and hydrogen abstraction of **III** aided by $O_2^{\bullet-}$ occurs to form $HO_2\cdot$ and intermediate **IV**, which finally transformed to the final product **3a** and H_2O_2. To further verify the possible mechanism, the by-product H_2O_2 was detected by iodometric experiments (supplementary Fig. 20†).

Conclusions

In summary, we developed a highly efficient Rh-catalyzed one-pot cascade strategy to synthesize robust non-substituted quinoline linked COFs directly from simple or readily available precursors. It was found that the dehydrating agent MgSO$_4$ played a pivotal role in adjusting the reaction balance between formation of reversible imine and irreversible annulation. In comparison with the "stop-and-go" PSM strategy developed in our previous work, the OPR strategy presented herein not only avoided the isolation of intermediates and featured operational friendliness, but also enabled COFs to be obtained with higher crystallinity and specific surface areas. The later merits led the NQ-COFs prepared by OPR to exhibit stronger visible-light absorption and carrier transfer ability, which contributed to the facile generation of the active species $O_2^{\bullet-}$. As a result, the NQ-COFs prepared by OPR were ascertained to be more efficient photocatalysts in the $O_2^{\bullet-}$-mediated coupling reaction for synthesizing a variety of 2-

benzimidazole derivatives. Furthermore, the general applicability of this OPR strategy was demonstrated by constructing 12 other NQ-COFs with different topologies and pore sizes. The approach reported in this work will reduce the difficulty in synthesizing stable COFs and thus promote COFs to find wide application in the future.

Experimental section

Typical procedure for the one-pot synthesis of NQ-COF$_{A1}$-OPR

A Pyrex glass tube (10 mL) was charged with aldehyde **A** (19.5 mg, 0.05 mmol), amine **1** (17.6 mg, 0.05 mmol), vinylene carbonate (38.7 mg, 0.45 mmol), acetic acid (HOAc, 0.05 mL), MgSO$_4$ (72 mg), mesitylene (0.5 mL), and 1,4-dioxane (1.0 mL). Subsequently, the tube was sonicated for 10 minutes, degassed by three freeze–pump–thaw cycles (liquid nitrogen), and sealed under vacuum. After being heated in an oven at 120 °C for 3 days, the cooled suspension was centrifuged to separate the solid, which was repeatedly washed with THF and water until the solvent was colourless. **NQ-COF$_{A1}$-OPR** was finally obtained as a brown powder (36 mg, 95%) after being dried under vacuum at 80 °C.

Typical procedure for the synthesis of 2-phenyl-1*H*-benzo[*d*]imidazole

A 10 mL Schlenk tube equipped with a stir bar was charged with *o*-phenylenediamine **1** (0.5 mmol), aldehyde **2** (0.5 mmol), **NQ-COF$_{A1}$-OPR** (5 mg), EtOH (1.0 mL), and H$_2$O (1.0 mL). After being subjected to evacuation/purging with O_2 for 10 min, the reaction mixture was irradiated in the photoreactor (18 W blue LEDs, 460–465 nm) with a cooling fan for 24 h under an O_2 atmosphere. After the reaction ended, the solid was collected by filtration, and the concentrated filtrate was purified by flash chromatography on silica gel with PE/EA as the eluent to afford the products.

Data availability

The datasets supporting this article have been uploaded as part of the ESI.†

Author contributions

Y.-G. Xiang conceived and designed the whole project, and H.-J. Pang conducted the synthesis of COFs and photocatalytic activity evaluation. Y.-Q. Zhu and X.-D. Zhao helped in parts of the structural characterization, and H.-J. Pang, D.-K. Huang, and Y.-G. Xiang participated in the writing of the paper.

Conflicts of interest

There are no conflicts to declare.

Acknowledgements

References

1 A. P. Cote, A. I. Benin, N. W. Ockwig, M. O'Keeffe, A. J. Matzger and O. M. Yaghi, *Science*, 2005, **310**, 1166–1170.

2 K. Geng, T. He, R. Liu, S. Dalapati, K. T. Tan, Z. Li, S. Tao, Y. Gong, Q. Jiang and D. Jiang, *Chem. Rev.*, 2020, **120**, 8814–8933.

3 S. Karak, K. Dey and R. Banerjee, *Adv. Mater.*, 2022, e2202751.

4 Y. Yusran, Q. Fang and V. Valtchev, *Adv. Mater.*, 2020, **32**, e2002038.

5 Y. Zhang, R. L. Zhong, M. Lu, J. H. Wang, C. Jiang, G. K. Gao, L. Z. Dong, Y. Chen, S. L. Li and Y. Q. Lan, *ACS Cent. Sci.*, 2021, **7**, 175–182.

6 Z. Guo, H. Wu, Y. Chen, S. Zhu, H. Jiang, S. Song, Y. Ren, Y. Wang, X. Liang, G. He, Y. Li and Z. Jiang, *Angew. Chem., Int. Ed.*, 2022, **61**, e202210466.

7 J. A. Martin-Illan, J. A. Suarez, J. Gomez-Herrero, P. Ares, D. Gallego-Fuente, Y. Cheng, D. Zhao, D. Maspoch and F. Zamora, *Adv. Sci.*, 2022, **9**, e2104643.

8 G. Das, B. Garai, T. Prakasam, F. Benyettou, S. Varghese, S. K. Sharma, F. Gándara, R. Pasricha, M. Baias, R. Jagannathan, N. i. Saleh, M. Elhabiri, M. A. Olson and A. Trabolsi, *Nat. Commun.*, 2022, **13**, 3904.

9 F. Yu, J. H. Ciou, S. Chen, W. C. Poh, J. Chen, J. Chen, K. Haruethai, J. Lv, D. Gao and P. S. Lee, *Nat. Commun.*, 2022, **13**, 390.

10 D. Bessinger, L. Ascherl, F. Auras and T. Bein, *J. Am. Chem. Soc.*, 2017, **139**, 12035–12042.

11 W. Dong, Y. Yang, Y. Xiang, S. Wang, P. Wang, J. Hu, L. Rao and H. Chen, *Green Chem.*, 2021, **23**, 5797–5805.

12 R. Chen, J. L. Shi, Y. Ma, G. Lin, X. Lang and C. Wang, *Angew. Chem., Int. Ed.*, 2019, **58**, 6430–6434.

13 M. Traxler, S. Gisbertz, P. Pachfule, J. Schmidt, J. Roeser, S. Reischauer, J. Rabeah, B. Pieber and A. Thomas, *Angew. Chem., Int. Ed.*, 2022, **61**, e202117738.

14 S. Trenker, L. Grunenberg, T. Banerjee, G. Savasci, L. M. Poller, K. I. M. Muggli, F. Haase, C. Ochsenfeld and B. V. Lotsch, *Chem. Sci.*, 2021, **12**, 15143–15150.

15 A. Jati, K. Dey, M. Nurhuda, M. A. Addicoat, R. Banerjee and B. Maji, *J. Am. Chem. Soc.*, 2022, **144**, 7822–7833.

16 S. Kandambeth, K. Dey and R. Banerjee, *J. Am. Chem. Soc.*, 2019, **141**, 1807–1822.

17 E. Q. Jin, M. Asada, Q. Xu, S. Dalapati, M. A. Addicoat, M. A. Brady, H. Xu, T. Nakamura, T. Heine, Q. H. Chen and D. L. Jiang, *Science*, 2017, **357**, 673–676.

18 S. Xu, H. Sun, M. Addicoat, B. P. Biswal, F. He, S. Park, S. Paasch, T. Zhang, W. Sheng, E. Brunner, Y. Hou, M. Richter and X. Feng, *Adv. Mater.*, 2021, **33**, e2006274.

19 S. Bi, F. Meng, D. Wu and F. Zhang, *J. Am. Chem. Soc.*, 2022, **144**, 3653–3659.

20 X. Guan, H. Li, Y. Ma, M. Xue, Q. Fang, Y. Yan, V. Valtchev and S. Qiu, *Nat. Chem.*, 2019, **11**, 587–594.

21 C. Zhao, H. Lyu, Z. Ji, C. Zhu and O. M. Yaghi, *J. Am. Chem. Soc.*, 2020, **142**, 14450–14454.

22 J. Maschita, T. Banerjee, G. Savasci, F. Haase, C. Ochsenfeld and B. V. Lotsch, *Angew. Chem., Int. Ed.*, 2020, **59**, 15750–15758.

23 H. Duan, K. Li, M. Xie, J. M. Chen, H. G. Zhou, X. Wu, G. H. Ning, A. I. Cooper and D. Li, *J. Am. Chem. Soc.*, 2021, **143**, 19446–19453.

24 F. Haase and B. V. Lotsch, *Chem. Soc. Rev.*, 2020, **49**, 8469–8500.

25 L. Cusin, H. Peng, A. Ciesielski and P. Samori, *Angew. Chem., Int. Ed.*, 2021, **60**, 14236–14250.

26 Z. B. Zhou, X. H. Han, Q. Y. Qi, S. X. Gan, D. L. Ma and X. Zhao, *J. Am. Chem. Soc.*, 2022, **144**, 1138–1143.

27 H. L. Nguyen, C. Gropp, N. Hanikel, A. Mockel, A. Lund and O. M. Yaghi, *ACS Cent. Sci.*, 2022, **8**, 926–932.

28 H. L. Qian, F. L. Meng, C. X. Yang and X. P. Yan, *Angew. Chem., Int. Ed.*, 2020, **59**, 17607–17613.

29 P. J. Waller, S. J. Lyle, T. M. O. Popp, C. S. Diercks, J. A. Reimer and O. M. Yaghi, *J. Am. Chem. Soc.*, 2016, **138**, 15519–15522.

30 F. Haase, E. Troschke, G. Savasci, T. Banerjee, V. Duppel, S. Dorfler, M. M. J. Grundei, A. M. Burow, C. Ochsenfeld, S. Kaskel and B. V. Lotsch, *Nat. Commun.*, 2018, **9**, 2600.

31 V. Singh, J. Kim, B. Kang, J. Moon, S. Kim, W. Y. Kim and H. R. Byon, *Adv. Energy Mater.*, 2021, **11**, 2003735.

32 X. R. Ren, B. Bai, Q. Zhang, Q. Hao, Y. Guo, L. J. Wan and D. Wang, *J. Am. Chem. Soc.*, 2022, **144**, 2488–2494.

33 X. Li, C. Zhang, S. Cai, X. Lei, V. Altoe, F. Hong, J. J. Urban, J. Ciston, E. M. Chan and Y. Liu, *Nat. Commun.*, 2018, **9**, 2998.

34 X. Zhao, H. Pang, D. Huang, G. Liu, J. Hu and Y. Xiang, *Angew. Chem., Int. Ed.*, 2022, e202208833.

35 Y. Yang, L. Yu, T. Chu, H. Niu, J. Wang and Y. Cai, *Nat. Commun.*, 2022, **13**, 2615.

36 J. M. Seo, H. J. Noh, H. Y. Jeong and J. B. Baek, *J. Am. Chem. Soc.*, 2019, **141**, 11786–11790.

37 H. Y. Liu, J. Chu, Z. L. Yin, X. Cai, L. Zhuang and H. X. Deng, *Chem*, 2018, **4**, 1696–1709.

38 S. J. Lyle, T. M. Osborn Popp, P. J. Waller, X. Pei, J. A. Reimer and O. M. Yaghi, *J. Am. Chem. Soc.*, 2019, **141**, 11253–11258.

39 P. F. Wei, M. Z. Qi, Z. P. Wang, S. Y. Ding, W. Yu, Q. Liu, L. K. Wang, H. Z. Wang, W. K. An and W. Wang, *J. Am. Chem. Soc.*, 2018, **140**, 4623–4631.

40 D. A. Pyles, J. W. Crowe, L. A. Baldwin and P. L. McGrier, *ACS Macro Lett.*, 2016, **5**, 1055–1058.

41 J. Liu, T. Yang, Z. P. Wang, P. L. Wang, J. Feng, S. Y. Ding and W. Wang, *J. Am. Chem. Soc.*, 2020, **142**, 20956–20961.

42 P. L. Wang, S. Y. Ding, Z. C. Zhang, Z. P. Wang and W. Wang, *J. Am. Chem. Soc.*, 2019, **141**, 18004–18008.

43 K. Wang, Z. Jia, Y. Bai, X. Wang, S. E. Hodgkiss, L. Chen, S. Y. Chong, X. Wang, H. Yang, Y. Xu, F. Feng, J. W. Ward and A. I. Cooper, *J. Am. Chem. Soc.*, 2020, **142**, 11131–11138.

44 N. Huang, K. H. Lee, Y. Yue, X. Xu, S. Irle, Q. Jiang and D. Jiang, *Angew. Chem., Int. Ed.*, 2020, **59**, 16587–16593.

45 M. Wang, M. Ballabio, M. Wang, H. H. Lin, B. P. Biswal, X. Han, S. Paasch, E. Brunner, P. Liu, M. Chen, M. Bonn, T. Heine, S. Zhou, E. Canovas, R. Dong and X. Feng, *J. Am. Chem. Soc.*, 2019, **141**, 16810–16816.

46 X. Wang, L. Chen, S. Y. Chong, M. A. Little, Y. Wu, W.-H. Zhu, R. Clowes, Y. Yan, M. A. Zwijnenburg, R. S. Sprick and A. I. Cooper, *Nat. Chem.*, 2018, **10**, 1180–1189.

47 S. Dadwal, M. Kumar and V. Bhalla, *J. Org. Chem.*, 2020, **85**, 13906–13919.